Photocurrent and photoluminescence mapping of Au/FA0.9MA0.1PbI3 junctions: Probing carrier diffusion and thermo-optical degradation

Jiazhuo Nie, Zhelu Hu, Alexandre Zimmers, Zhuoying Chen, Lionel Aigouy

Photocurrent and Photoluminescence Mapping of Au/$FA_{0.9}MA_{0.1}PbI_3$ Junctions: Probing Carrier Diffusion and Thermo-Optical Degradation

Jiazhuo Nie[1], *Zhelu Hu*[2], *Alexandre Zimmers*[1], *Zhuoying Chen*[1], *Lionel Aigouy*[1]

[1] Laboratoire de Physique et d'Etude des Matériaux (LPEM), CNRS, ESPCI Paris, PSL Research University, Sorbonne Université, 10 rue Vauquelin, F-75231 Paris, France

[2] State Key Laboratory of Flexible Electronics (LoFE) & Institute of Advanced Materials (IAM), School of Flexible Electronics (Future Technologies), Nanjing Tech University, Nanjing, 211816, China

Corresponding author: lionel.aigouy@espci.fr

ABSTRACT

We present a combined photocurrent (PC) and photoluminescence (PL) imaging study of $FA_{0.9}MA_{0.1}PbI_3$ perovskite thin films patterned with Au gold pads forming planar Schottky junctions. From these measurements, we extract a room temperature carrier diffusion length between 6 and 10 µm, consistent with previous results on pure $MAPbI_3$ compounds. This value decreases by a factor of 2-3 when the device temperature is raised to 75°C. Interestingly, after two hours of thermal stress at this temperature in ambient air, both the optical and electrical responses return to their initial levels upon cooling to room temperature, indicating reversible behavior and confirming the good thermal stability of this material at moderate operating conditions. In contrast, localized high-power laser illumination leads to irreversible degradation, characterized by the disappearance of both PL and PC signals. These results suggest that such material can tolerate global short term temperature elevations without any permanent damage, such as those encountered under sunlight exposure.

Journal of Applied Physics

AIP Publishing

I. INTRODUCTION

Hybrid metal halide perovskites have recently emerged as very promising materials for optoelectronic applications, like for instance solar cells, photodetectors, and light-emitting devices.[1-5] In the field of photon detection, they exhibit strong optical absorption and, despite their polycrystalline structure when they are in the form of a thin film, possess long carrier diffusion lengths and high tolerance to defects, which together allow efficient charge generation and extraction. These exceptional optical and transport properties have led to the design of devices with very high power conversion efficiency (PCE) exceeding 25%.[6-9] However, a comprehensive understanding of charge transport and recombination at the microscale remains essential for improving device performance and stability, particularly regarding the effects of external stresses such as temperature elevation on material properties, which can lead to accelerated degradation and reduced operational lifetime. In this work, we investigate the carrier diffusion length and the thermal-stress resilience of formamidinium methylammonium lead iodide ($FA_{0.9}MA_{0.1}PbI_3$) thin films, which is a derivative of the mixed-cation perovskite methylammonium lead iodide ($MAPbI_3$). Such material is supposed to have a better thermal stability than the single organic cation variant $MAPbI_3$[10,11] which makes it of particularly interest for the development of stable, long-life and more efficient mixed-cation perovskite-based solar cells.

To determine the carrier diffusion length, we chose to use scanning photocurrent (PC) microscopy[12-19] which, unlike other optical techniques such as time-resolved photoluminescence (TRP), provides a direct and spatially resolved measurement of carrier diffusion in planar device geometries. Although it does not replicate the vertical architecture of real solar cells, it allows to directly infer the diffusion length from the spatial variations of PC and reveals local differences linked to eventual structural or electronic inhomogeneities, even in apparently homogeneous films. In addition, since PC relies on local excitation with a tightly focused laser beam, photon absorption also generates a spatially resolved photoluminescence signal (PL). Simultaneous measurement of PC and PL therefore provides complementary information on charge carriers, distinguishing between those that diffuse and contribute to the photocurrent and those that recombine radiatively, thereby adding an extra dimension to the analysis.

From the PC maps, we will first determine the carrier diffusion length of $FA_{0.9}MA_{0.1}PbI_3$ at room temperature in a planar device configuration with Au electrodes, which form two equivalent junctions. The PC images will then be analyzed as a function of modulation frequency, applied bias across the double-junction structure, temperature, and controlled degradation induced by a high-power laser spot. In conjunction with PL measurements, this approach will provide comprehensive insights into the material's stability under stress conditions.

II. EXPERIMENTAL METHODS

$FA_{0.9}MA_{0.1}PbI_3$ film was synthesized on top of a glass substrate via a two-step method in an N_2-filled glove box, in accordance with our previous work.[20] 1.5M PbI_2 was dissolved in anhydrous DMF/DMSO (9:1, v/v) under stirring and spin-coated onto the glass substrate at 1500 rpm for 30s, followed by annealing at 70°C for 1 min. After cooling to room temperature, a second precursor solution of FAI:MAI:MACl = 90mg:9mg:9mg in 1 mL IPA was spin-coated at 2000 rpm for 30s onto the PbI_2 film and then annealed at 150°C for 15 min to form the homogeneous perovskite layer. The gold electrodes with channel widths of 50 µm and 20 µm were thermally evaporated through a shadow mask.

The experimental setup for combined PC-PL is shown in Fig. 1a. It is basically derived from a homemade near and far-field multipurpose scanning microscope.[21-22] The sample is mounted on a Peltier heating device equipped with a Pt100 resistance temperature sensor for temperature monitoring. The Peltier element is controlled by a Belektronig BTC temperature controller to regulate the sample temperature. The assembly is positioned on a piezoelectric XYZ translation stage (Nanocube, Physik Instrumente) for precise spatial scanning. The setup is integrated into an optical microscope (Olympus BH2) and illuminated by a focused 447 nm laser beam (Coherent Bioray) through a high numerical aperture (NA) objective (Olympus LMPlanFL ×100, NA = 0.8), producing a ~ 1 µm wide excitation spot. To increase the sensitivity of the PC and PL measurements, the laser intensity is modulated. Both signals are simultaneously recorded using two lock-in amplifiers (EG&G Instruments Model 7260), with PL detection performed by a photomultiplier tube (Hamamatsu Photonics). The scanning through the stage motion and the signal acquisition are synchronized by a custom LabVIEW program to obtain spatially resolved PC and PL maps. For the experiments presented in the next section, the laser power was kept at a minimum value (specified later in the text) in order to avoid heating the material and create thermoelectric effect. An optical image of the junction with the focused laser spot is shown in Fig. 1b. For electrical measurements, the gold pads were connected either to a Keithley 2612B source measurement unit (SMU) to perform I(V) curves, either to a power supply (Tektronix PWS4305) placed in series with the lock-in amplifier to apply a bias to the junction (Fig. 1a) during the scans. One-sun illumination was provided by a class ABB (ASTM E927-10) Newport LCS-100 solar simulator with an AM 1.5G filter.

III. RESULTS AND DISCUSSION

Figure 1c and 1d show the I(V) characteristics of the device, measured in the dark and under illumination. The nonlinear response indicates that the structure does not behave as an ohmic contact, but rather as a back-to-back Schottky junction, with each Au/ $FA_{0.9}MA_{0.1}PbI_3$ interface acting as a single rectifying contact. This behavior is consistent with the well-studied Au/$MAPbI_3$ interface, known to form an n-type Schottky

junction (see Figure 1e) where the Au work function (~ 5.1 eV) induces upward band bending and an electron-injection barrier at the interface.[23-25] Under illumination, the current increases significantly and exhibits a clear photovoltaic response, confirming efficient photogeneration and separation of charge carriers within the perovskite layer.

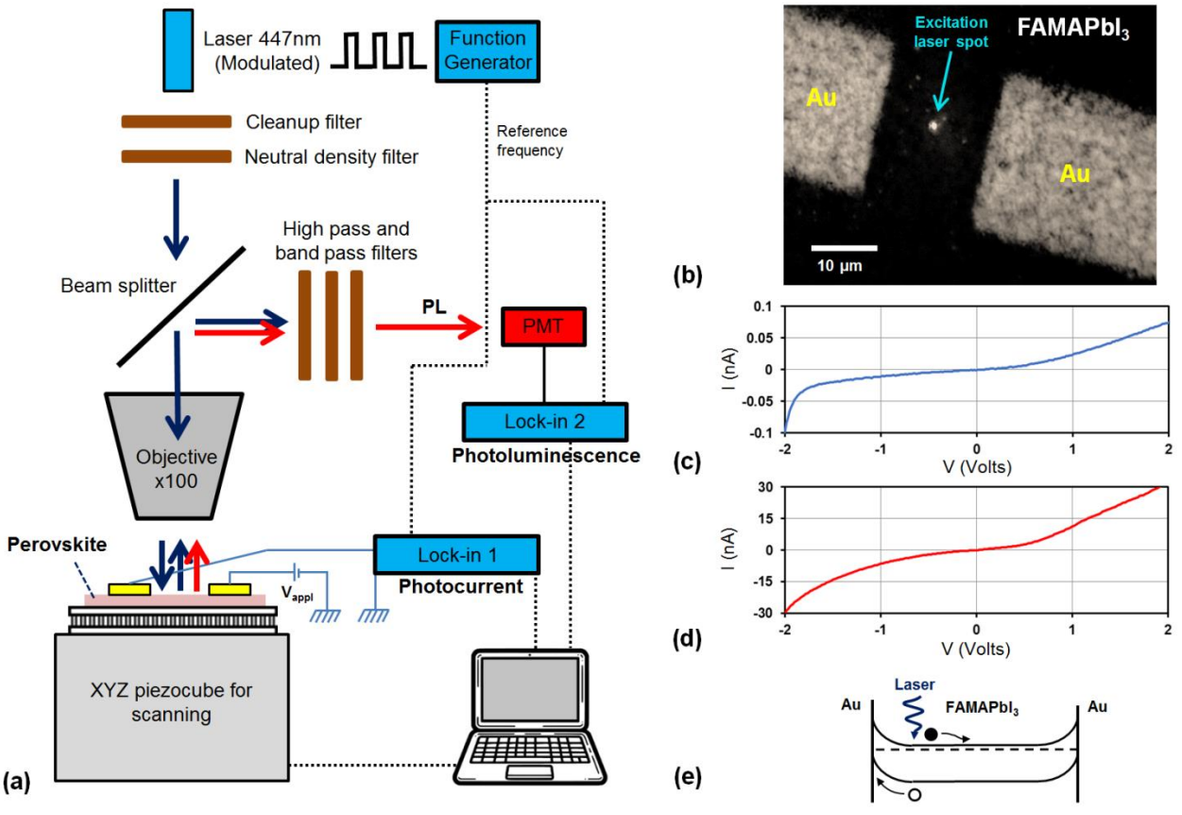

Figure 1: Experimental setup (a); optical micrograph of the junction (b); current–voltage characteristics measured in the dark (c) and under 1-sun illumination (d); schematic representation of the back-to-back Schottky junction (e).

Figure 2 displays the PC and PL maps of two devices of different geometry at zero bias. The samples, further referred as samples A and B, have a junction width of 50 µm and 20 µm respectively. The incident laser power was around 5 µW, focused on a ~1 µm wide spot, for both samples, with a laser intensity-modulated at 1530 Hz for sample A and 731 Hz for sample B. The PL maps follow the sample geometry, showing strong emission from the perovskite region and no signal from the Au pads. In contrast, the PC maps reveal two asymmetric regions, with a positive photocurrent on one side and a negative photocurrent of similar amplitude on the opposite side. The reversed current sign measured near the two metal contacts is due to

the definition of one of the current flow directions as positive. The maximum photocurrent (positive or negative) appears near the metal contacts and vanishes near the center of the junction. This antisymmetric pattern is typical of PC measurements and has been previously reported for various systems, including carbon nanotubes,[12] graphene transistors,[13] nanowire FETs,[16-18] PbSe quantum-dot FETs,[19] and perovskite thin films.[26-42] Upon local illumination, electron–hole pairs are generated and diffuse within the perovskite layer. When excitation occurs close to a contact, one type of carrier is preferentially driven toward the electrode by the local built-in field, giving rise to a measurable current. Illumination near the opposite electrode produces a current of opposite polarity, consistent with the device symmetry. In our case, the photocurrent is negative near the pad connected to the positive terminal of the amperemeter and positive on the opposite side, indicating that electrons are collected at the Au contacts and possibly associated with upward band bending at the Au/$FA_{0.9}MA_{0.1}PbI_3$ interfaces (Figure 1e).

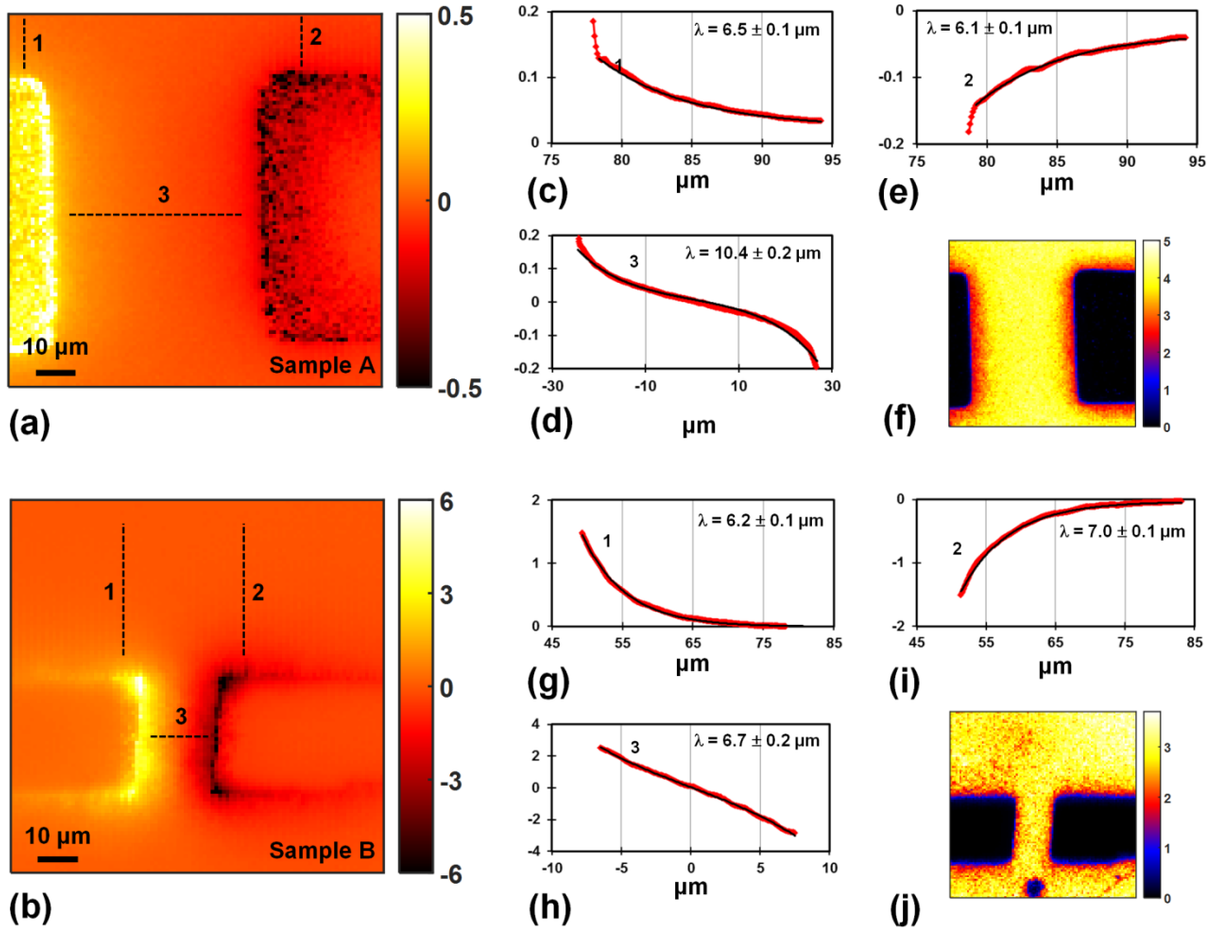

Figure 2: Photocurrent maps (in nA) of two different junctions [(a) and (b)] and corresponding photoluminescence maps [(f) and (j)]. Panels (c), (d), and (e) show experimental cross-sections (red dotted lines) extracted from the photocurrent map in (a), together with the corresponding fits (black solid lines). Panels (g), (h), and (i) show the same analysis for the photocurrent map in (b).

Figure 2 shows the PC cross-sections of the two devices extracted from various directions, between the electrodes (cross-section 3), and in directions perpendicular to the junction (cross-sections 1 and 2). Although built-in fields may exist near the Au/perovskite interfaces, their spatial extent is assumed to be much smaller than the scanned distances. The photocurrent decay is therefore considered to be dominated by carrier diffusion in the present analysis. As mentioned previously, after the photogeneration, the electrons and holes can move in the layer, in a simple diffusive way since there is no bias. If the carriers do not find an obstacle and do not recombine, they can travel toward an electrode, be collected and create the current. The PC signal decreases exponentially when the distance between the electrode and the generation zone increases, like the equation: [14,15]

$$I_{PC} = I_0 \cdot e^{-\frac{x}{\lambda}} \quad (1)$$

where x is the distance to the electrode, λ is the minority carrier diffusion length equaled to $\sqrt{D\tau}$ where D is the diffusion constant and τ is the carrier lifetime, and I_0 is a constant that depends on the amount of carriers that have been photogenerated. Since there are two electrodes, if the electrodes are close to each other, then between them, we can extrapolate and approximate the current that flows in the circuit as:

$$I_{PC} = I_2 - I_1 = I_0 \cdot \left[e^{-\frac{|x+x_0|}{\lambda}} - e^{-\frac{|x-x_0|}{\lambda}} \right] \quad (2)$$

Here, I_1 and I_2 are the photocurrent generated in each electrode, x_0 denotes the distance between the device center and the electrodes and x denotes the distance between the illumination spot and the device center. At the center of the junction (x = 0), the net photocurrent is zero, because the contributions from both electrodes cancel each other. For the junctions shown in Fig.2, we extracted the carrier diffusion length by fitting the PC profiles between the electrodes using equation (2) and outside the electrodes using equation (1). From these fits (black lines in Fig. 2c-e and Fig. 2g-i), we obtain diffusion lengths ranging between 6 µm and 10 µm for all investigated samples, depending on the junction geometry and on the sample growth conditions that can vary from one batch to another. The uncertainty due to the fit itself is also given and is smaller than 0.2 µm in the analyzed samples. Table 1 summarizes diffusion lengths λ reported found in the literature for similar perovskite materials. These are widely dispersed, spanning from about 1 µm in polycrystalline thin films to several tens of micrometers in single crystals. The diffusion lengths measured here on $FA_{0.9}MA_{0.1}PbI_3$ are comparable to those reported for $MAPbI_3$ and $MAPbI_{3-x}Cl_x$, indicating that partial substitution of MA by FA does not significantly affect the electrical transport properties of these structures.

The measurements were performed using a modulated laser excitation at a frequency of 1531 Hz for sample A and 731 Hz for sample B. We verified that the modulation frequency has no measurable influence on either the amplitude of the photocurrent or the extracted diffusion length. The difference in photocurrent

amplitude observed between samples A and B mainly arises from differences in device geometry (electrode size and junction width) and from the fact that the samples were fabricated in different batches, which can affect light absorption efficiency and overall photoresponse. To further assess the influence of the modulation frequency, we measured the photocurrent amplitude as a function of frequency. The corresponding data are presented in Fig. S1 of the Supplementary Material and show no significant variation over the investigated frequency range. This behavior indicates that the measured PC is not dominated by a photothermoelectric contribution. Indeed, local laser heating could, in principle, generate temperature gradients and induce thermoelectric currents that affect carrier transport. However, as discussed in Ref. 45, such photothermoelectric effects are frequency-dependent, since heat dissipation and thermal diffusion vary with modulation frequency. In that case, the PC amplitude would be expected to decrease with increasing frequency, which is not observed here. We therefore conclude that the measured signal originates from the intrinsic diffusion of photogenerated carriers in the material, under zero applied bias.

Material	Form	Method	Diffusion length (μm)	Reference
$CH_3NH_3PbI_3$	Thin film	PL Quenching, Time-resolved PL	0.1-0.12	Shrank et al[30]
$CH_3NH_3PbI_{3-x}Cl_x$	Thin film	PL Quenching, Time-resolved PL	1-1.2	Shrank et al[30]
$CH_3NH_3PbI_3$	Thin film	Transient THz spectroscopy (TTS), Time-resolved terahertz spectroscopy (TRTS)	1	Wehrenfennig et al[31]
$CH_3NH_3PbI_{3-x}Cl_x$	Thin film	TTS, TRTS	2-3	Wehrenfennig et al[31]
$CH_3NH_3PbI_3$	Thin film	Transient absorption microscopy (TAM)	1.2	Guo et al[32]
$CH_3NH_3PbI_3$	SC	Transient photovoltage (TPV) Impedance Spectroscopy (IS)	> 175	Dong et al[33]
$CH_3NH_3PbI_3$	NWs/NPs	Time resolved, PL Imaging	14	Tian et al[34]
$CH_3NH_3PbBr_3$	NWs/NPs	Time resolved, PL Imaging	6	Tian et al[34]
$CH_3NH_3PbI_3$	NWs/NPs	SPCM	21	Xiao et al[35]
$CH_3NH_3PbI_3$	Thin film	SPCM	10	Liu et al[29]
$CH_3NH_3PbI_3$	SC	SPCM Time-resolved microwave conductivity (TRMC)	10-28 (e-) 27-65 (h+)	Semonin et al[36]
$CH_3NH_3PbI_3$	Thin film / powder	Surface Photovoltage (SPV)	0.2-15.5	Dittrich et al[37]
$CH_3NH_3PbI_3$	Thin film	Femto four wave mixing (FWM)	0.95	Webber et al[38]
$CH_3NH_3PbI_3$	Thin film	SPCM	50	Kim et al[26]
$CH_3NH_3PbI_{3-x}Cl_x$	Thin film	SPCM	8.5	Kim et al[26]
$CH3NH_3PbBr_3$	SC-MC	Two-photons SPCM	7.5	Yang et al[39]
$CH_3NH_3PbI_3$	SC	SPCM	10-25	Shrestha et al[27]
$CH_3NH_3PbI_3$	SC	SPCM	10-200	McClintock et al[40]
$FACsPbI_3$	Thin film	Laser-illuminated microwave microscopy (LMIM)	3-5	Ma et al[41]
$CH_3NH_3PbI_3$	2D perov	SPCM	7-18	Shrestha et al[28]
$GAFAPbI_3$	SC	I(V) on variable thicknesses	600	Lv et al[42]

$CH_3NH_3PbI_3$	Thin SC	Time of flight (TOF) Space-Charged limited current (SPLC) Photoconductivity	82.7	Liu et al[43]
$FACsPbI_3$	Thin film	TAM	0.7-1.4	Xie et al[44]

Table 1: Diffusion lengths reported in the literature for single- and mixed-cation perovskites, together with the corresponding measurement techniques. NW = nanowires, NP = nanoplates, SC = single crystals.

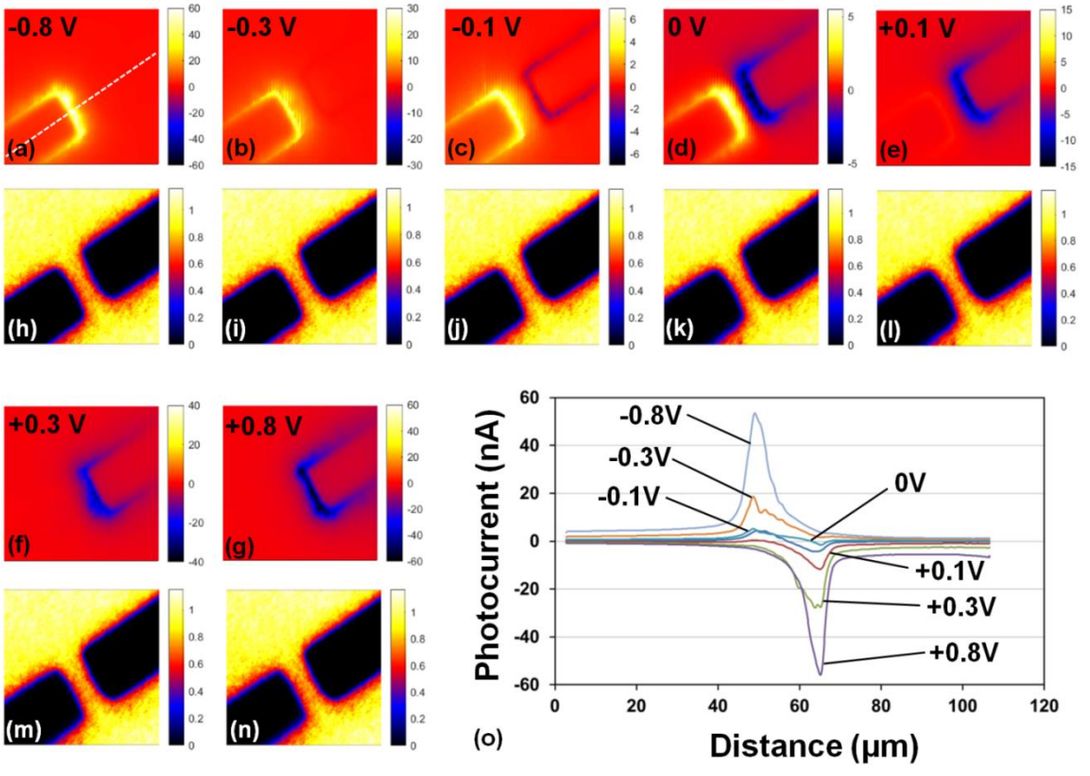

Figure 3: Photocurrent maps (in nA) of a junction acquired at different biases V_{appl} [(a)–(g)] and corresponding photoluminescence maps [(h)–(n)]. Panel (o) shows cross-sections extracted from the photocurrent maps along the white dashed line indicated in (a). The image size is 90 μm × 90 μm.

We next applied an external bias V_{appl} to the junction. In this configuration, charge carriers are drifted by the external electric field, and the two electrodes are no longer electrically equivalent. Figures 3a–g and 3h–n show the photocurrent and photoluminescence maps, respectively, recorded as a function of the applied bias, ranging from −0.8 V to +0.8 V. The device has a geometry similar to that of sample B. At zero bias, the PC map exhibits an almost perfect antisymmetry (due to the positive definition of the current flow direction) with respect to the center of the junction. Upon applying a bias, this antisymmetry is progressively broken,

and photogenerated carriers are preferentially driven toward one side of the junction, depending on the polarity of the applied voltage. As the bias increases, the electric field across the junction becomes stronger, leading to a corresponding increase in the photocurrent amplitude. This behavior is consistent with previous observations reported in Refs. 26 and 27. At applied voltages of ±0.8 V, the photocurrent reaches values exceeding ±50 nA, which is approximately an order of magnitude larger than the maximum photocurrent measured at zero bias (Figure 3o). In this regime, drift transport adds to, and eventually dominates over, the natural diffusion of carriers. In contrast, the simultaneously acquired PL maps do not show any noticeable changes over the entire range of applied biases. This indicates that neither the radiative recombination of photogenerated carriers nor their overall recombination dynamics are significantly affected by the applied electric field, despite the strong enhancement of carrier drift.

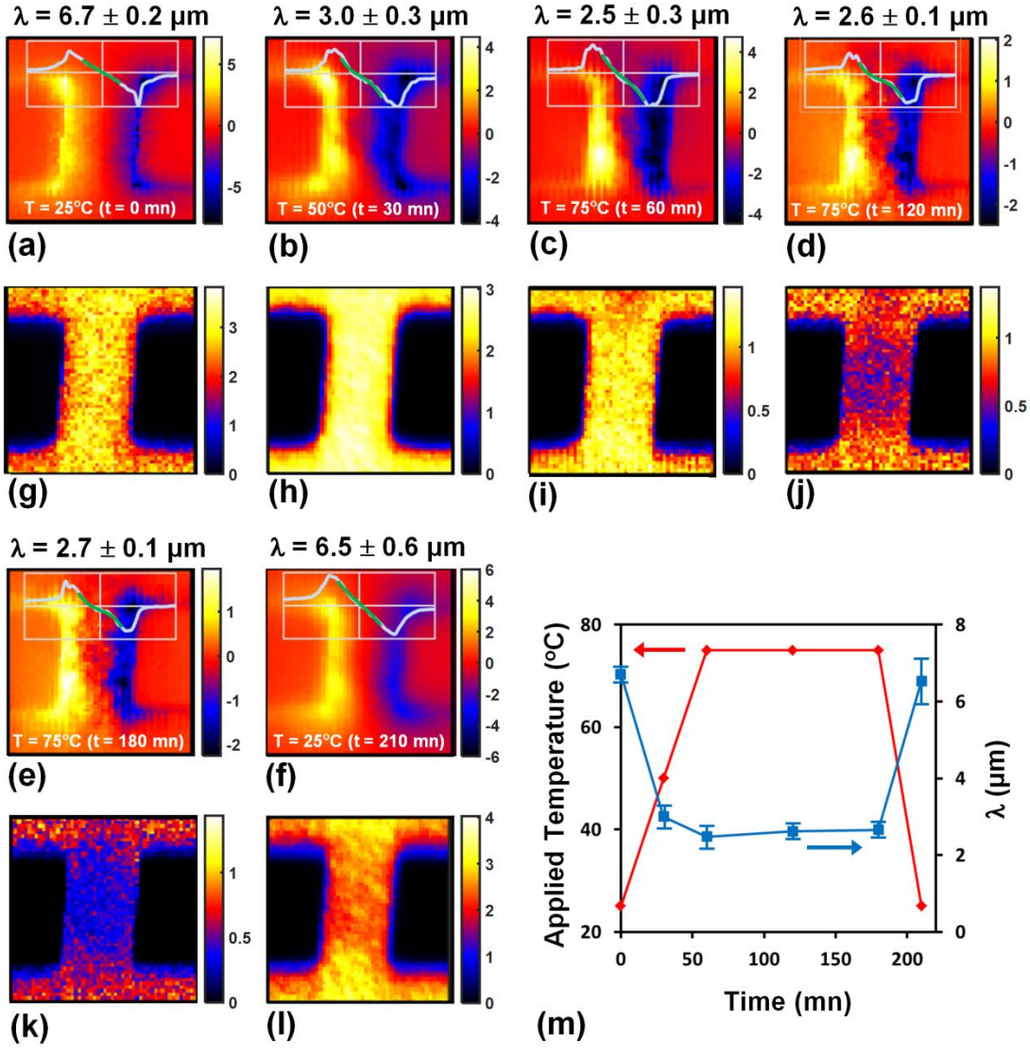

Figure 4: Photocurrent maps (in nA) [(a)–(f)] and corresponding photoluminescence maps [(g)–(l)] of a junction acquired at different temperatures and times. Insets show cross-sections extracted from the photocurrent images, with experimental data (cyan curves) and fits using Eq. (2) (green curves). The image size is 50 µm × 50 µm. The extracted diffusion lengths λ are indicated at the top of each image. Panel (m) shows the evolution of the diffusion length as a function of time and temperature.

The previous bias-dependent study, which required several hours of scanning, demonstrated that the junctions did not degrade over such time, nor under low laser excitation power, nor upon application of an external electric field. We next investigated the influence of temperature on the PC and PL maps. A junction with geometry similar to previous samples was mounted on a Peltier stage under the microscope and heated to 50 °C and 75 °C. These temperatures are low enough to preserve the structural integrity of the material, while being sufficiently high to noticeably affect its electronic transport properties and carrier dynamics. The corresponding PC and PL maps are presented in Fig. 4(a–f) and Fig. 4(g–l), respectively. During this series of experiments, care was taken to ensure that the measurement conditions were the same, particularly regarding laser focusing and unwanted thermal drift. At all temperatures, the antisymmetric shape of the SPCM maps is preserved, with positive and negative photocurrent signals collected on opposite electrodes. The main differences appear in the photocurrent cross-sections and in the corresponding fits. The extracted diffusion length λ decreases from 6.7 $\pm$ 0.2 µm at room temperature (25 °C) to approximately 2.5 $\pm$ 0.3 µm at 75 °C (Figure 4a-c). This reduction can be attributed to a decrease in charge-carrier mobility and to the activation of temporary trap states that shorten the carrier lifetime.[46] This behavior is consistent with the results of Milot *et al.*,[46] who reported a decrease in both mobility and diffusion length in $MAPbI_3$, from about 2.5 µm at 22 °C to 1.2 µm at 67 °C. In the present case, a comparable reduction in diffusion length is observed for $FA_{0.9}MA_{0.1}PbI_3$ over a similar temperature range.

To evaluate the temporal stability at elevated temperature, the sample was maintained at 75 °C and the PC and PL maps were recorded again after one hour and then after two hours. As shown in Fig. 4c-e, the extracted diffusion length remains identical, with values close to 2.5 µm, even under prolonged exposure at 75 °C. In contrast, a decrease in the maximum PC amplitude, together with a reduction in PL intensity, is observed between the first scan at 75 °C and subsequent scans at the same temperature (Figure 4c-e and 4i-k). Both the PC and PL intensity are reduced by approximately a factor of two, indicating the onset of thermal degradation and bleaching of the material. This decrease in radiative recombination and current generation is also accompanied by the appearance of darker localized regions within the junction. Finally, the sample was cooled back down to room temperature, and the PL and PC maps were measured again (Figure 4f and 4i). Remarkably, both the PC and the PL maximum values are recovered and the diffusion length returns to a value of about 6.5 $\pm$ 0.6 µm, close to its initial value (Figure 4m). These observations, and

particularly the recovery of the initial properties, indicate that $FA_{0.9}MA_{0.1}PbI_3$ is relatively robust against moderate thermal stress, even after a prolonged exposure at 75°C, despite a temporary decrease of the optical and electrical response. Such behavior is consistent with previous reports showing that MA-poor or MA-free compositions, such as pure $FAPbI_3$ or Cs-stabilized FA-based perovskites, exhibit improved thermal and structural stability under comparable conditions.[47] In particular, FA cations have been shown to be more resilient to thermal degradation, and although decomposition processes may occur,[48] they are largely reversible when the temperature remains below approximately 95 °C, as is the case in this study.

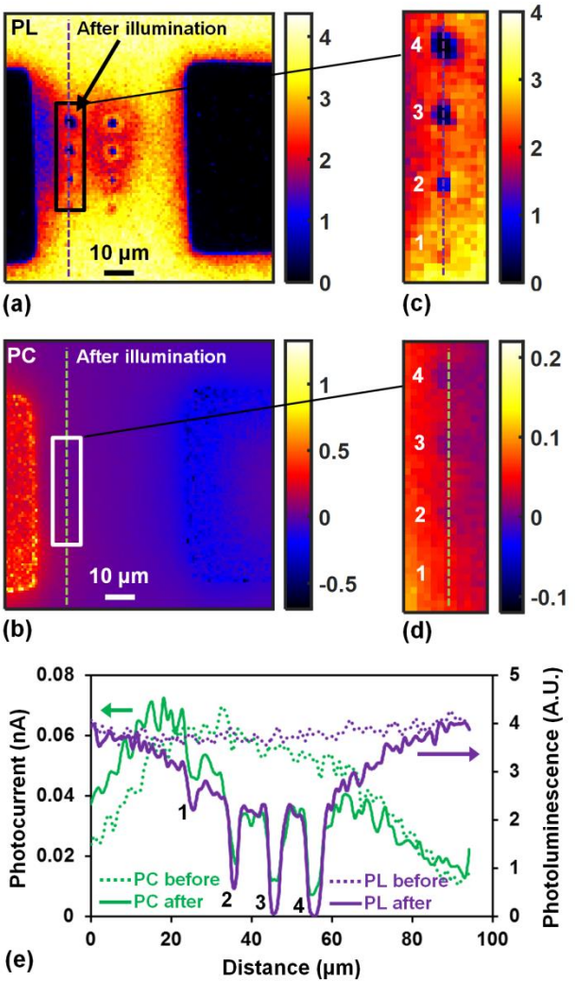

Figure 5: Photoluminescence [(a), (c)] and corresponding photocurrent [(b), (d)] maps of a junction after local illumination with a focused laser beam. The dark spots indicate the regions of local illumination. Cross-sections extracted from the images are shown in (e). Dotted and solid lines correspond to PL and PC signals before and after illumination, respectively.

Naturally, this robustness has limits. To probe these limits, we performed local high-power laser illumination experiments. The results are summarized in Fig. 5 (see Figure S2 of the supplementary materials for more details). A localized region of the junction, between the electrodes, was illuminated for 8 min at progressively increasing laser power densities: 0.06 mW/µm² (zone 1), 0.34 mW/µm² (zone 2), 0.61 mW/µm² (zone 3), and 0.89 mW/µm² (zone 4). After this exposure, a low-power scan (5 µW/µm²) was performed to assess the impact of the local illumination (Fig. 5a-d). As evidenced in the maps, zoomed images, and cross-sections, both the PL and PC signals are locally altered, with damage becoming more pronounced as the laser power density increases. A detailed identification of the degradation mechanisms would require local structural and chemical analyses (e.g., X-ray or spectroscopic probes), which are not accessible at the spatial scale of these experiments. However, extensive studies on larger areas have shown that, in $MAPbI_3$, prolonged illumination, especially under UV or blue light, induces degradation through progressive material dissociation, leading to the formation of PbI_2 grains or needles and volatile organic species.[49-52] Similar degradation pathways are likely to be operative in $FA_{0.9}MA_{0.1}PbI_3$ under intense local illumination.

IV. SUMMARY AND CONCLUSION

In this work, we investigated charge-carrier transport and thermal-stress resilience in $FA_{0.9}MA_{0.1}PbI_3$ thin films using scanning photocurrent microscopy combined with simultaneous photoluminescence mapping. At room temperature, carrier diffusion lengths ranging from 6 to 10 µm were extracted, comparable to those reported for $MAPbI_3$ - based perovskites, indicating that partial substitution of MA by FA does not significantly alter transport properties. Bias-dependent measurements show a transition from diffusion-dominated to drift-dominated transport without affecting radiative recombination and with an excellent stability with time. Upon increasing the temperature up to 75 °C, the diffusion length decreases to 2.5 µm, consistent with reduced mobility and shorter carrier lifetimes, in agreement with literature. Importantly, despite a temporary reduction in photocurrent and photoluminescence intensity at elevated temperature, the diffusion length fully recovers its value upon cooling back to room temperature. These results demonstrate the robustness and good reversibility of the optical and electrical transport properties of $FA_{0.9}MA_{0.1}PbI_3$ under moderate thermal stress, while high-power local illumination reveals the limits of this stability through irreversible degradation.

SUPPLEMENTARY MATERIAL SECTION

Journal of Applied Physics

AIP Publishing

More information on the preparation of the perovskite sample, the frequency dependence of the photocurrent maps, and the analysis of the laser-induced degradation are given in the supplementary material.

ACKNOWLEDGMENTS

Z.C. and L.A. acknowledge the support from the PEPR TASE "MINOTAURE" project (ANR-22-PETA-0015) and the "NBG_SolarCells" (ANR-24-CE05-7657) project.

AUTHOR DECLARATIONS SECTION

Conflict of Interest

The authors have no conflicts to disclose.

Author Contributions

Jiazhuo Nie: Conceptualization (equal); Formal analysis (equal); Data curation (equal); Investigation (equal); Writing – review & editing (equal). Zhelu Hu: Conceptualization (equal); Investigation (equal); Writing – review & editing (equal). Alexandre Zimmers: Conceptualization (equal); Investigation (equal); Formal analysis (equal); Writing – review & editing (equal). Zhuoying Chen: Conceptualization (equal); Funding acquisition (lead); Supervision (equal); Writing – review & editing (equal). Lionel Aigouy: Conceptualization (lead); Investigation (equal); Formal analysis (equal); Resources (equal); Supervision (equal); Writing – original draft (lead) ; Writing – review & editing (equal).

DATA AVAILABILITY

The data that support the findings of this study are available from the corresponding authors upon reasonable request.

REFERENCES

[1] A. Kojima, K. Teshima, Y. Shirai, T. Miyasaka, Organometal Halide Perovskites as Visible-Light Sensitizers for Photovoltaic Cells, J. Am. Chem. Soc. 131 (2009), 6050-6051. https://doi.org/10.1021/ja809598r

[2] L. Dou, Y. Yang, J. You, Z. Hong, W.-H. Chang, G. Li, Y. Yang, Solution-processed hybrid perovskite photodetectors with high detectivity, Nat. Commun. 5 (2014), 5404. https://doi.org/10.1038/ncomms6404

[3] J. Y. Kim, J.-W. Lee, H. S. Jung, H. Shin, N.-G. Park, High-Efficiency Perovskite Solar Cells, Chem. Rev. 120 (2020), 7867-7918. https://doi.org/10.1021/acs.chemrev.0c00107

[4] C. Yang, W. Hu, J. Liu, C. Han, Q. Gao, A. Mei, Y. Zhou, F. Guo, H. Han, Achievements, challenges, and future prospects for industrialization of perovskite solar cells, Light Sci. Appl. 13 (2024), 227. https://doi.org/10.1038/s41377-024-01461-x

[5] G. Li, Z. Su, L. Canil, D. Hughes, M.H. Aldamasy, J. Dagar, S. Trofimov, L. Wang, W. Zuo, J. J. Jerónimo-Rendon, M. M. Byranvand, C. Wang, R. Zhu, Z. Zhang, F. Yang, G. Nasti, B. Naydenov, W. C. Tsoi, Z. Li, X. Gao, Z. Wang, Y. Jia, E. Unger, M. Saliba, M. Li, A. Abate, Highly efficient p-i-n perovskite solar cells that endure temperature variations, Science 379 (2023), 399-403. https://doi.org/10.1126/science.add7331

[6] J. Zhou, L. Tan, Y. Liu, H. Li, X. Liu, M. Li, S. Wang, Y. Zhang, C. Jiang, R. Hua, W. Tress, S. Meloni, C. Yi, Highly efficient and stable perovskite solar cells via a multifunctional hole transporting material, Joule 8 (2024), 1691-1706. https://doi.org/10.1016/j.joule.2024.02.019

[7] M. A. Green, E. D. Dunlop, G. Siefer, M. Yoshita, N. Kopidakis, K. Bothe, X. Hao, Solar cell efficiency tables (Version 61), Prog. Photovoltaics Res. Appl. *31 (2023*), 3-16. https://doi.org/10.1002/pip.3646

[8] F. Cao, L. Bian, L. Li, Perovskite solar cells with high-efficiency exceeding 25%: A review, Energy Mater. Devices 2 (2024), 9370018. https://doi.org/10.26599/EMD.2024.9370018

[9] Z. Xiong, Q. Zhang, K. Cai, H. Zhou, Q. Song, Z. Han, S. Kang, Y. Li, Q. Jiang, X. Zhang, J. You, Homogenized chlorine distribution for >27% power conversion efficiency in perovskite solar cells, Science 390 (2025), 638-642. https://doi.org/10.1126/science.adw8780

[10] F. Ma, J. Li, W. Li, N. Lin, L. Wang, J. Qiao, Stable α/δ phase junction of formamidinium lead iodide perovskites for enhanced near-infrared emission, Chem. Sci. 8 (2017), 800-805. https://doi.org/10.1039/C6SC03542F

[11] V. Held, N. Mrkyvkova, Y. Halahovets, P. Nádaždy, K. Vegso, A. Vlk, M. Ledinský, M. Jergel, S. Bernstorff, J. Keckes, F. Schreiber, P. Siffalovic, Evolution of Defects, Morphology, and Strain during FAMAPbI3 Perovskite

Vacuum Deposition: Insights from In Situ Photoluminescence and X-ray Scattering, ACS Appl. Mater. Interfaces 16 (2024), 35723-35731. https://doi.org/10.1021/acsami.4c04095

[12] K. Balasubramanian, M. Burghard, K. Kern, M. Scolari, A. Mews, Photocurrent Imaging of Charge Transport Barriers in Carbon Nanotube Devices, Nano Lett. 5 (2005), 507-510. https://doi.org/10.1021/nl050053k

[13] F. Xia, T. Mueller, R. Golizadeh-Mojarad, M. Freitag, Y. Lin, J. Tsang, V. Perebeinos, P. Avouris, Photocurrent Imaging and Efficient Photon Detection in a Graphene Transistor Nano Lett. 9 (2009), 1039-1044. https://doi.org/10.1021/nl8033812

[14] R. Graham, D. Yu, Scanning Photocurrent Microscopy in Semiconductor Nanostructures, Mod. Phys. Lett. B 27 (2013), 1330018. https://doi.org/10.1142/S0217984913300184

[15] R. Xiao, Y. Hou, M. Law, D. Yu, On the Use of Photocurrent Imaging To Determine Carrier Diffusion Lengths in Nanostructured Thin-Film Field-Effect Transistors, J. Phys. Chem. *C* 122 (2018), 18356-18364. https://doi.org/10.1021/acs.jpcc.8b06734

[16] R. Graham, C. Miller, E. Oh, D. Yu, Electric Field Dependent Photocurrent Decay Length in Single Lead Sulfide Nanowire Field Effect Transistors, Nano Lett. 11 (2011), 717–722. https://doi:10.1021/nl1038456

[17] D. Fu, J. Zou, K. Wang, R. Zhang, D. Yu, J. Wu, Electrothermal Dynamics of Semiconductor Nanowires under Local Carrier Modulation, Nano Lett. 11 (2011), 3809–3815. https://doi:10.1021/nl2018806

[18] Y. Ahn, J. Dunning, J. Park, Scanning Photocurrent Imaging and Electronic Band Studies in Silicon Nanowire Field Effect Transistors, Nano Lett. 5 (2005), 1367–1370. https://doi:10.1021/nl050631x

[19] T. Otto, C. Miller, J. Tolentino, Y. Liu, M. Law, D. Yu, Gate-dependant Carrier Diffusion Length in Lead Selenide Quantum Dot Field Effect Transistors, Nano Lett. 13 (2013), 3463–3469. https://doi:10.1021/nl401698z

[20] J. Nie, D. Zhang, H. Xiang, T. Pons, L. Aigouy, Z. Chen, Nanothermometry-guided In Situ Decoding of Perovskite Solar Cell Degradation under Optical Stress, Nano Energy 144 (2025), 111405. https://doi:10.1016/j.nanoen.2025.111405

[21] H. Xiang, H.-J. Lin, T. Niu, Z. Chen, L. Aigouy, Nanoscale Thermal Characterization of High Aspect Ratio Gold Nanorods for Photothermal Applications at λ = 1.5 µm, J. Appl. Phys. 125 (2019), 163101. https://doi.org/10.1063/1.5088944

[22] H.-J. Lin, H. Xiang, C. Xin, Z. Hu, L. Billot, P. Gredin, M. Mortier, Z. Chen, M.-U. González, A. García-Martín, L. Aigouy, Direct Imaging of Fluorescence Enhancement in the Gap between Two Gold Nanodisks, Appl. Phys. Lett. 118 (2021), 161105. https://doi.org/10.1063/5.0049395

[23] X. Liu, C. Wang, L. Lyu, C. Wang, Z. Xiao, C. Bi, J. Huang, Y. Gao, Electronic Structures at the Interface between Au and $CH_3NH_3PbI_3$, Phys. Chem. Chem. Phys. 17 (2015), 896–902. https://doi:10.1039/c4cp03842h

[24] Y.-F. Chen, Y.-T. Tsai, D. M. Bassani, R. Clerc, D. Forgács, H. J. Bolink, M. Wussler, W. Jaegermann, G. Wantza, L. Hirsch, Evidence of Band Bending Induced by Hole Trapping at $MAPbI_3$ Perovskite/Metal Interface, J. Mater. Chem. A 4 (2016), 17529–17536. https://doi:10.1039/C6TA08979H

[25] K. Hong, K. C. Kwon, K. S. Choi, Q. V. Le, S. J. Kim, J. S. Han, J. M. Suh, S. Y. Kim, C. M. Sutter-Fella, H. W. Jang, Strong Fermi-Level Pinning at Metal Contacts to Halide Perovskites, J. Mater. Chem. C 9 (2021), 15212–15220. https://doi.org/10.1039/D1TC03370K

[26] A. Kim, B. H. Son, H. S. Kim, Y. H. Ahn, Direct Measurement of Diffusion Length in Mixed Lead-Halide Perovskite Films Using Scanning Photocurrent Microscopy, Curr. Opt. Photonics 2 (2018), 514–518. https://doi.org/10.3807/COPP.2018.2.6.514

[27] S. Shrestha, H. Tsai, M. Yoho, D. Ghosh, F. Liu, Y. Lei, J. Tisdale, J. K. Baldwin, S. Xu, A. J. Neukirch, S. Tretiak, D. Vo, W. Nie, The Role of Metal-Semiconductor Interface in Halide Perovskite Devices for Radiation Photon Counting, ACS Appl. Mater. Interfaces 12 (2020), 45533–45540. https://doi:10.1021/acsami.0c11805

[28] S. Shrestha, X. Li, H. Tsai, C.-H. Hou, H.-H. Huang, D. Ghosh, J.-J. Shyue, L. Wang, S. Tretiak, X. Ma, W. Nie, Long Carrier Diffusion Length in Two-Dimensional Lead Halide Perovskite Single Crystals, Chem 8 (2022), 1107–1120. https://doi:10.1016/j.chempr.2022.01.008

[29] S. Liu, L. Wang, W.-C. Lin, S. Sucharitakul, C. Burda, X. P. A. Gao, Imaging the Long Transport Lengths of Photogenerated Carriers in Oriented Perovskite Films, Nano Lett. 16 (2016), 7925–7929. https://doi:10.1021/acs.nanolett.6b04235

[30] S. D. Stranks, G. Eperon, G. Grancini, C. Menelaou, M. J. P. Alcocer, T. Leijtens, L. M. Herz, A. Petrozza, H. J. Snaith, Electron-Hole Diffusion Lengths Exceeding 1 Micrometer in an Organometal Trihalide Perovskite Absorber, Science 342 (2013), 341–344. https://doi:10.1126/science.1243982

[31] C. Wehrenfennig, G. Eperon, M. B. Johnston, H. J. Snaith, L. M. Herz, High Charge Carrier Mobilities and Lifetimes in Organolead Trihalide Perovskites, Adv. Mater. 26 (2014), 1584–1589. https://doi:10.1002/adma.201305172

[32] Z. Guo, J. S. Manser, Y. Wan, P. V. Kamat, L. Huang, Spatial and Temporal Imaging of Long-Range Charge Transport in Perovskite Thin Films by Ultrafast Microscopy, Nat. Commun. 6 (2015), 7471. https://doi:10.1038/ncomms8471

[33] Q. Dong, Y. Fang, Y. Shao, P. Mulligan, J. Qiu, L. Cao, J. Huang, Electron-Hole Diffusion Lengths > 175 μm in Solution-Grown $CH_3NH_3PbI_3$ Single Crystals, Science 347 (2015), 967–970. https://doi:10.1126/science.aaa5760

[34] W. Tian, C. Zhao, J. Leng, R. Cui, S. Jin, Visualizing Carrier Diffusion in Individual Single-Crystal Organolead Halide Perovskite Nanowires and Nanoplates, J. Am. Chem. Soc. 137 (2015), 12458–12461. https://doi.org/10.1021/jacs.5b08045

[35] R. Xiao, Y. Hou, Y. Fu, X. Peng, Q. Wang, E. Gonzalez, S. Jin, D. Yu, Photocurrent Mapping in Single-Crystal Methylammonium Lead Iodide Perovskite Nanostructures, Nano Lett. 16 (2016), 7710–7717. https://doi:10.1021/acs.nanolett.6b03782

[36] O. E. Semonin, G. A. Elbaz, D. B. Straus, T. D. Hull, D. W. Paley, A. M. van der Zande, J. C. Hone, I. Kymissis, C. R. Kagan, X. Roy, J. S. Owen, Limits of Carrier Diffusion in n-Type and p-Type $CH_3NH_3PbI_3$ Perovskite Single Crystals, J. Phys. Chem. Lett. 7 (2016), 3510–3518. https://doi:10.1021/acs.jpclett.6b01308

[37] Th. Dittrich, F. Lang, O. Shargaieva, J. Rappich, N. H. Nickel, E. Unger, B. Rech, Diffusion Length of Photo-Generated Charge Carriers in Layers and Powders of $CH_3NH_3PbI_3$ Perovskite, Appl. Phys. Lett. 109 (2016), 073901. https://doi.org/10.1063/1.4960641

[38] D. Webber, C. Clegg, A. W. Mason, S. A. March, I. G. Hill, K. C. Hall, Carrier Diffusion in Thin-Film $CH_3NH_3PbI_3$ Perovskite Measured Using Four-Wave Mixing, Appl. Phys. Lett. 111 (2017), 121905. https://doi.org/10.1063/1.4989970

[39] B. Yang, J. Chen, Q. Shi, Z. Wang, M. Gerhard, A. Dobrovolsky, I. G. Scheblykin, K. J. Karki, K. Han, T. Pullerits, High Resolution Mapping of Two-Photon Excited Photocurrent in Perovskite Micro-Plate Photodetector, J. Phys. Chem. Lett. 9 (2018), 5017–5022. https://doi:10.1021/acs.jpclett.8b02250

[40] L. McClintock, R. Xiao, Y. Hou, C. Gibson, H. C. Travaglini, D. Abramovitch, L. Z. Tan, R. T. Senger, Y. Fu, S. Jin, D. Yu, Temperature and Gate Dependence of Carrier Diffusion in Single Crystal Methylammonium Lead Iodide Perovskite Microstructures, J. Phys. Chem. Lett. 11 (2020), 1000–1006. https://doi:10.1021/acs.jpclett.9b03643

[41] X. Ma, F. Zhang, Z. Chu, J. Hao, X. Chen, J. Quan, Z. Huang, X. Wang, X. Li, Y. Yan, K. Zhu, K. Lai, Superior Photo-Carrier Diffusion Dynamics in Organic-Inorganic Hybrid Perovskites Revealed by Spatiotemporal Conductivity Imaging, Nat. Commun. 12 (2021), 5009. https://doi:10.1038/s41467-021-25311-1

[42] M. Lv, N. Li, G. Jin, X. Du, X. Tao, Z. Chen, Phase-Stable $FAPbI_3$-Based Single Crystals with 600-μm Electron Diffusion Length, Matter 6 (2023), 4388–4400. https://doi:10.1016/j.matt.2023.10.021

[43] D. Liu, Y. Zheng, X. Y. Sui, X. F. Wu, C. Zou, Y. Peng, X. Liu, M. Lin, Z. Wei, H. Zhou, Y.-F. Yao, S. Dai, H. Yuan, H. G. Yang, S. Yang, Y. Hou, Universal Growth of Perovskite Thin Monocrystals from High Solute Flux for Sensitive Self-Driven X-Ray Detection, Nat. Commun. 15 (2024), 2390. https://doi:10.1038/s41467-024-46712-y

[44] J. Xie, W. Zhou, H. Li, Z. Wang, J. Jiang, Y. Zhang, X. Shen, Z. Ning, W. Liu, Visualizing Carrier Diffusion in Cs-Doping $FAPbI_3$ Perovskite Thin Films Using Transient Absorption Microscopy, Adv. Optical Mater. 12 (2024), 2303004. https://doi:10.1002/adom.202303004

[45] X. Wang, H. Gao, Distinguishing the Photothermal and Photoinjection Effects in Vanadium Dioxide Nanowires, Nano Lett. 15 (2015), 7037–7042. https://doi:10.1021/acs.nanolett.5b03086

[46] R. L. Milot, G. Eperon, H. J. Snaith, M. B. Johnston, L. M. Herz, Temperature Dependent Charge Carrier Dynamics in $CH_3NH_3PbI_3$ Perovskite Thin Films, Adv. Funct. Mater. 25 (2015), 6218–6227. https://doi.org/10.1002/adfm.201502340

[47] K. Zhao, L. Yao, C. Değer, X. Zhang, J. Shen, X. Miao, P. Shi, Y. Luo, D. Jin, Y. Tian, J. Xu, S. Zhang, Q. Liu, S. Chu, X. Wang, L. Tian, I. Yavuz, J. Xue, R. Wang, Mitigating Residual MA^+ for Stable $FAPbI_3$ Perovskite Photovoltaics, Nat. Commun. 16 (2025), 10074. https://doi:10.1038/s41467-025-65045-y

[48] E. J. Juarez-Perez, L. K. Ono, Y. Qi, Thermal Degradation of Formamidinium Based Lead Halide Perovskites into Sym-Triazine and Hydrogen Cyanide Observed by Coupled Thermogravimetry-Mass Spectrometry Analysis, J. Mater. Chem. A 7 (2019), 16912–16919. https://doi:10.1039/C9TA06058H

[49] J. Wei, Q. Wang, J. Huo, F. Gao, Z. Gan, Q. Zhao, H. Li, Mechanisms and Suppression of Photoinduced Degradation in Perovskite Solar Cells, Adv. Energy Mater. 11 (2021), 2002326. https://doi:10.1002/aenm.202002326

[50] N. H. Nickel, F. Lang, V. V. Brus, O. Shargaieva, J. Rappich, Unraveling the Light-Induced Degradation Mechanisms of $CH_3NH_3PbI_3$ Perovskite Films, Adv. Electron. Mater. 3 (2017), 1700158. https://doi:10.1002/aelm.201700158

[51] G. Abdelmageed, L. Jewell, K. Hellier, L. Seymour, B. Luo, F. Bridges, J. Z. Zhang, S. Carter, Mechanisms for Light Induced Degradation in $MAPbI_3$ Perovskite Thin Films and Solar Cells, Appl. Phys. Lett. 109 (2016), 233905. https://doi:10.1063/1.4967840

[52] P.-C. Huang, T.-J. Yang, C.-J. Lin, M.-Y. Wang, W.-C. Lin, Unraveling the Heat- and UV-Induced Degradation of Mixed Halide Perovskite Thin Films via Surface Analysis Techniques, Langmuir 40 (2024), 11873–11887. https://doi:10.1021/acs.langmuir.3c03816